AGU PUBLICATIONS

JGR

Journal of Geophysical Research: Solid Earth

RESEARCH ARTICLE
10.1002/2015JB012379

Key Points:
- Multidisciplinary study of the Mount Etna 28 December 2014 dike-fed paroxysm
- Constraints on shallow dike emplacement and driving mechanisms at Mount Etna
- Relationship between drainage of shallow plumbing system and dike emplacement

Supporting Information:
- Texts S1–S4, Figures S1–S5, and Caption for Movie S1
- Movie S1

Correspondence to:
S. Gambino,
salvatore.gambino@ingv.it

Citation:
Gambino, S., A. Cannata, F. Cannavò, A. La Spina, M. Palano, M. Sciotto, L. Spampinato, and G. Barberi (2016), The unusual 28 December 2014 dike-fed paroxysm at Mount Etna: Timing and mechanism from a multidisciplinary perspective, *J. Geophys. Res. Solid Earth*, *121*, doi:10.1002/2015JB012379.

Received 21 JUL 2015
Accepted 5 FEB 2016
Accepted article online 11 FEB 2016

The unusual 28 December 2014 dike-fed paroxysm at Mount Etna: Timing and mechanism from a multidisciplinary perspective

Salvatore Gambino[1], Andrea Cannata[1,2], Flavio Cannavò[1], Alessandro La Spina[1], Mimmo Palano[1], Mariangela Sciotto[1], Letizia Spampinato[1], and Graziella Barberi[1]

[1]Istituto Nazionale di Geofisica e Vulcanologia, Sezione di Catania-Osservatorio Etneo, Catania, Italy, [2]Department of Physics and Geology, University of Perugia, Perugia, Italy

Abstract Between 2011 and 2013, there were 43 lava fountain episodes from Mount Etna's New South-East summit crater (NSEC). In 2014, this intense activity was supplanted by sporadic Strombolian explosions and the opening of an eruptive fissure between July and August. The only lava fountaining episode of the year occurred on 28 December; this was characterized by the emplacement of a shallow dike that, at the surface, fed two distinct lava flows from an ENE-WSW trending eruptive fissure. Here we provide a detailed picture of the onset of the dike emplacement, as well as the mechanism driving its migration, using a multidisciplinary data set based on seismic, geodetic, geochemical, and volcanological observations. The dike emplacement was preceded by a pressurization of the magmatic plumbing system recorded from August 2014 on. This pressurization has been modeled as a vertically elongated magmatic source located beneath the summit craters at ~4.5 km below sea level. From September to October, magma rising was also detected by seismic and geochemical data that highlighted pressurization of the shallower portion of the plumbing system. We suggest that the 28 December 2014 dike emplacement resulted from a modification of the preexisting NSEC shallow plumbing system, largely due to drainage of the main shallow conduit during the July–August 2014 eruptive fissure activity. Such a structural modification might have created the conditions for magma emplacement as a dike-like structure.

1. Introduction

Mount Etna is an open-vent basaltic volcano whose eruptive activity ranges from quiescent degassing from its summit craters to explosive and effusive phases from either its summit or flanks [*Branca and Del Carlo*, 2005]. Over time, the volcano has fed long-lasting effusive eruptions, commonly associated with weak explosive activity from its flanks, and short-lasting, more powerful explosive episodes ranging from strongly Strombolian to subplinian and usually accompanied by small lava flows [*Andronico and Lodato*, 2005; *Branca and Del Carlo*, 2005]. In particular, after the spectacular lava fountain paroxysms fed by the South-East crater (SEC) in 2000–2001 [e.g., *Andronico and Corsaro*, 2011; *La Spina et al.*, 2015] (inset in Figure 1a) and the 2001 and 2002–2003 eruptions producing both lava flows and explosive activity of variable intensity [e.g., *Acocella and Neri*, 2003; *Spampinato et al.*, 2008], between 2004 and 2006 Mount Etna's activity showed predominantly effusive eruptions [e.g., *Burton et al.*, 2005; *Andronico et al.*, 2009]. In 2007, episodic explosive activity and lava fountains were observed [e.g., *Andronico et al.*, 2008], with the last preceding the start of the 2008–2009 effusive eruption [e.g., *Aloisi et al.*, 2009; *Bonaccorso et al.*, 2011]. After the end of lava effusion, in January 2011, a new phase of explosive eruptions started [e.g., *Bonaccorso et al.*, 2013; *Spampinato et al.*, 2015]. This phase consisted of episodic short-lasting eruptions of predominantly explosive behavior [e.g., *Gouhier et al.*, 2012]. The eruptions were fed by a new summit crater (named New SEC or NSEC) that built up around a pit that had opened on the SEC eastern flank in late 2009 [e.g., *Behncke et al.*, 2014] (inset in Figure 1a).

Overall, from January 2011 and 2013, NSEC produced 43 lava fountain episodes (see *Patanè et al.* [2013], *De Beni et al.* [2015], and *Bonforte and Guglielmino* [2015] for chronology details). The episodes consisted of Strombolian activity of increasing intensity that eventually evolved into powerful lava fountaining [e.g., *Calvari et al.*, 2011; *Bonaccorso and Calvari*, 2013]. Some eruptive episodes displayed short transitional times, whereas others needed longer time to evolve into lava fountains [e.g., *Spampinato et al.*, 2015]. Further, this phase of activity was characterized by eruptive events of variable intensity. In the first half of 2014, the explosivity of NSEC decreased in intensity, and only a period of intense Strombolian activity on 21–27 January was observed; for the remaining time, mainly intracrater to mild

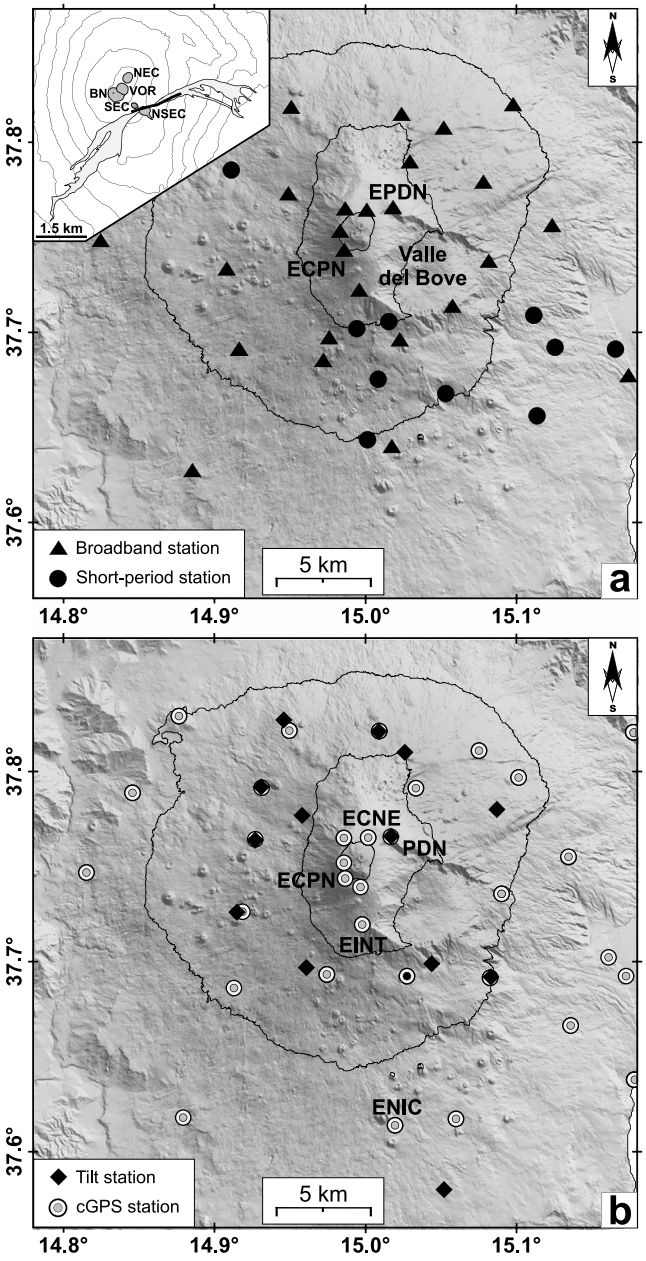

Figure 1. Shaded relief of Mount Etna volcano showing the location of the (a) seismic, and (b) GPS and tilt networks. The inset in Figure 1a shows the summit craters (NSEC: New South-East Crater; SEC: South-East Crater; NEC: North-East Crater; BN: Bocca Nuova; VOR: Voragine), the eruptive fissure that opened on 28 December 2014 (thick black line), and the associated lava flows (light grey areas) are also shown (redrawn from *Bonforte and Guglielmino* [2015]).

Strombolian activity was detected [*De Beni et al.*, 2015]. On 15 June 2014, intense Strombolian activity occurred at NSEC and preceded on 5 July, the opening of an eruptive fissure at ~3020 m above sea level (asl), which eventually fed Strombolian activity and lava flows until 10 August 2014 [*De Beni et al.*, 2015]. The development of dry fractures in the area between the eruptive fissure and the NSEC suggested that fissure activity was fed by the NSEC shallow magmatic system [*De Beni et al.*, 2015]. The location where the eruptive fissure developed was almost the same as previous effusive activity in 2008–2009 [e.g., *Bonaccorso et al.*, 2011]. The fissure followed the path of the dry segments of the 2008 fracture system [*Aloisi et al.*, 2009; *De Beni et al.*, 2015].

On 8 August 2014 weak Strombolian activity was observed at NSEC, and on 10 August a new eruptive fissure opened on its eastern flank; this episode marked the return of eruptive activity to the NSEC. This fissure produced a lava flow that spread toward Valle del Bove (Figure 1a) and vigorous Strombolian activity until the fourteenth of the same month. Eruptive activity at the NSEC ended on 16 August 2014, although intracrater explosions occurred weakly and discontinuously until early December 2014. On 28 December, the NSEC fed a new lava fountain episode, which was the only one in 2014 [*Bonforte and Guglielmino*, 2015].

In this study we focus on this last lava fountain that showed some peculiarities when compared with the previous activity at NSEC, namely the occurrence of dike emplacement [*Bonforte and Guglielmino*, 2015]. However, rather than focusing only on the dike modeling, here we also investigate the likely triggering mechanisms leading to the dike-fed lava fountain, especially considering the difference with the previous NSEC fountains that showed similar mechanisms [e.g., *Calvari et al.*, 2011; *Bonaccorso et al.*, 2013; *Patanè et al.*, 2013; *Viccaro et al.*, 2014; *Spampinato et al.*, 2015]. Specifically, we use integrated geophysical, geochemical, and volcanological observations, spanning the period from March 2014 to December 2014 to (i) model the dike, (ii) set the occurrence of this anomalous paroxysm in the framework of the lava fountains produced by NSEC in 2011–2013, and (iii) investigate the relationship between the July–August 2014 fissure eruption and the following December lava fountain.

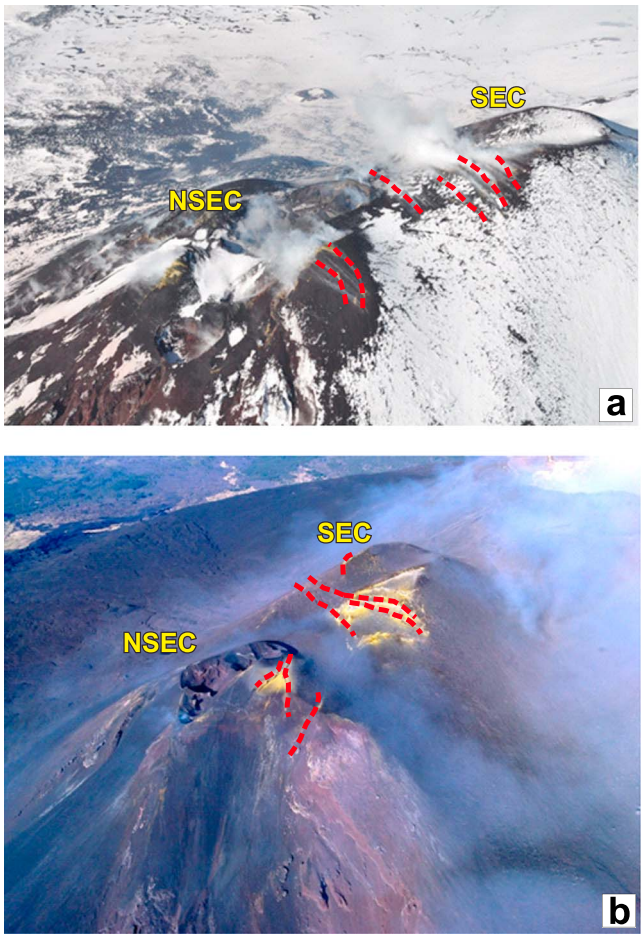

Figure 2. Photographs taken on (a) 8 April 2014 and on (b) 18 August 2014, showing the fracture field (highlighted with red dashed lines) opened at the summit of NSEC and between SEC and NSEC. Figures 2a and 2b are courtesy of S. Branca and Com. Piero Berti, Butterfly s.r.l. Helicopters Services, respectively.

2. The 28 December 2014 Lava Fountain Chronology

The 28 December 2014 lava fountain started abruptly at ~16:50 (all times are in Greenwich Mean Time) and intensified throughout the day. Poor weather conditions prevented any visual observation of the phenomenon, and the only evidences came from volcanic tremor (Figure S1 in the supporting information) and from ash fallout over the eastern sector of the volcano [*Bonforte and Guglielmino*, 2015]. The paroxysmal phase lasted about 2 h in all; volcanic tremor decreased after 18:30, and at ~21:00 the eruptive activity ended definitively. During the paroxysm, two distinct lava flow fields developed from a NE-SW trending eruptive fissure that opened between SEC and NSEC summits and emplaced in the upper part of the Valle del Bove (inset Figure 1a) [*Bonforte and Guglielmino*, 2015]. The eruptive fissure developed between the two SE craters, an area already affected by intense fracturing and fumarolic activity (Figure 2a). The degassing fractures were aligned in the N75°E direction and were distributed following an almost concentric concave pattern. The fractures in that zone were already observable at least since April 2014 (Figure 2a) and seemed to be more prominent in August 2014, in particular after the end of the fissure eruption (Figure 2b).

3. Data Analysis

3.1. Seismic Data

Seismic activity at Mount Etna is monitored by the permanent network of Istituto Nazionale di Geofisica e Vulcanologia, Sezione di Catania-Osservatorio Etneo (see supporting information for details).

3.1.1. Long-Term Analysis

Volcanic tremor and long period (LP) events were investigated during the period between 1 August and 31 December 2014. We investigated temporal and spatial variations in both amplitude and source centroid of volcanic tremor. The amplitude was estimated as RMS (root-mean-square) calculated over 10 min long time windows of the signal recorded by the vertical component of the EPDN station and filtered in the band 0.5–5.5 Hz (Figure 3a). The source of the centroid was located every 30 min by using an amplitude-based method [*Cannata et al.*, 2013]. Figure 4 shows source location results plotted in a map together with sections, as well as its temporal variation.

The detection of LP was performed by short-time-average over long-time-average algorithm on the seismic signals recorded at ECPN and EPDN. ECPN is the reference station for the characterization of LP events at Mount Etna [*Cannata et al.*, 2009, 2013]. The choice to consider the additional station EPDN was made after

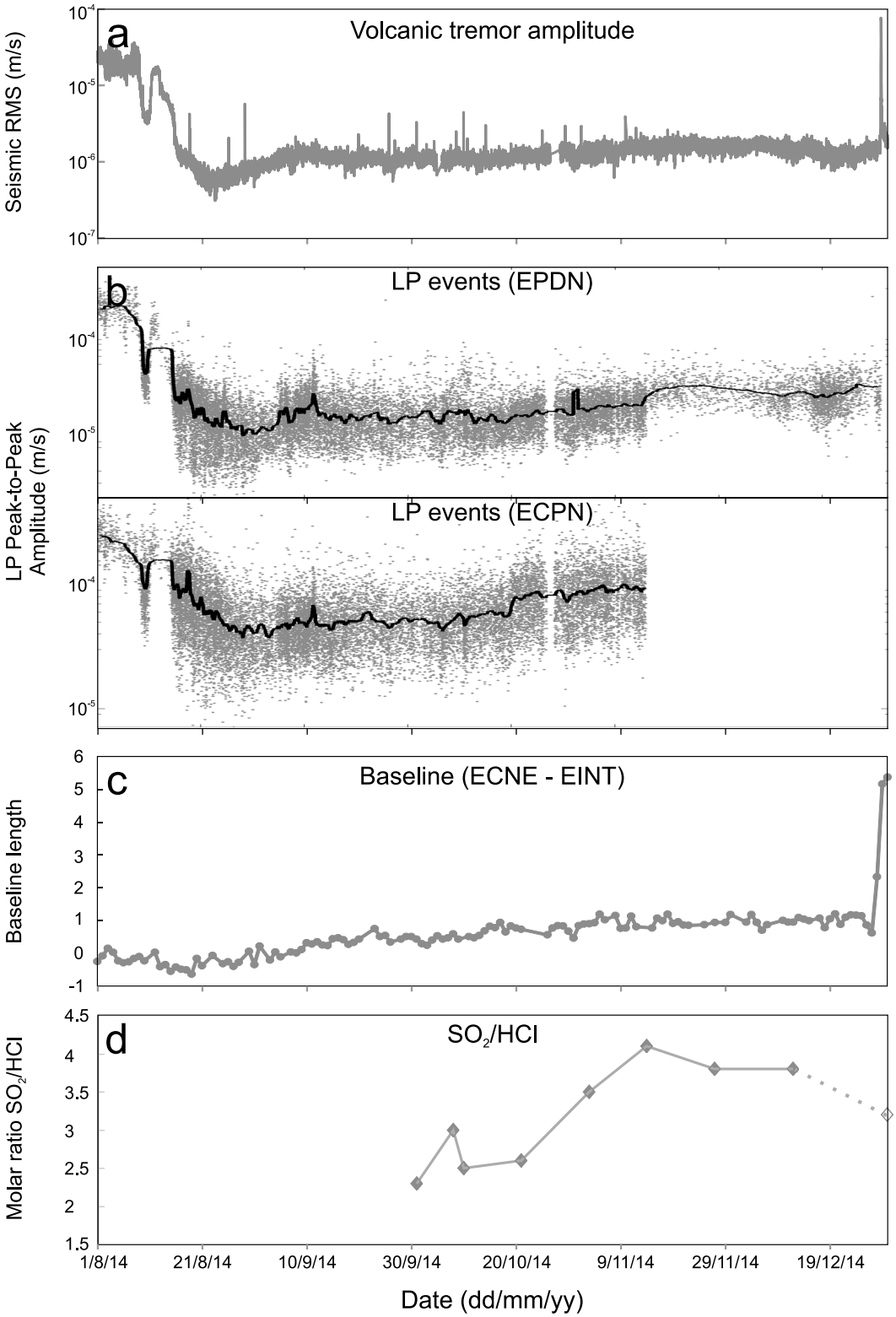

Figure 3. Variation in time (a) of the seismic RMS of the vertical component of the EPDN station, (b) of the peak-to-peak amplitude of the LP events measured at EPDN and ECPN stations, (c) of the length of the baseline ECNE-EINT, and (d) of the SO_2/HCl ratio, between 1 August and 31 December 2014.

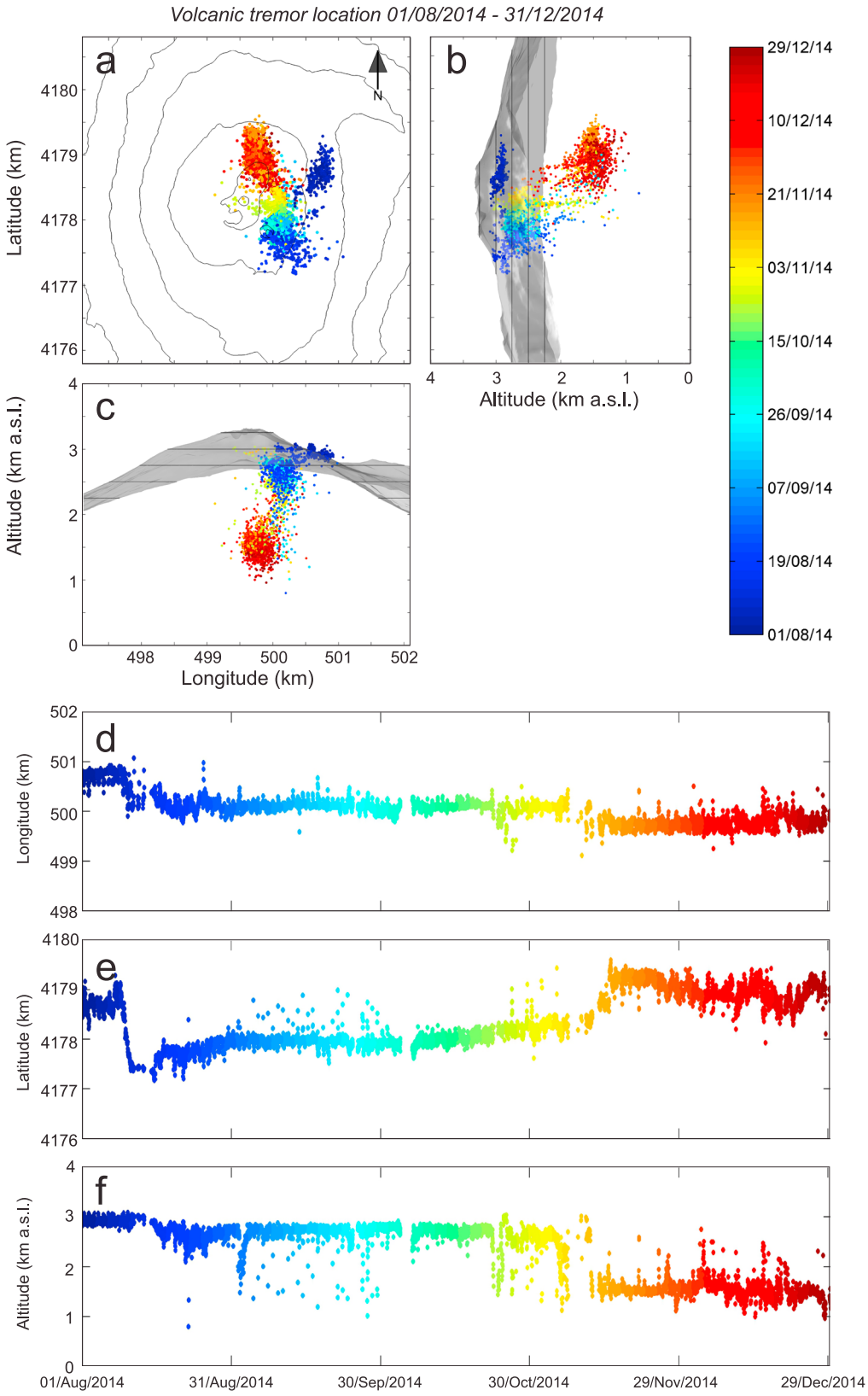

Figure 4. Spatial distribution of source centroids of volcanic tremor location plotted in (a) map and (b and c) sections of Mount Etna during 1 August to 31 December 2014 (the dot color indicates the event chronology according to the time color bar) and (d–f) corresponding time evolution.

ECPN stopped working on 15 November. Both peak-to-peak amplitude and source location were determined for each LP event. The amplitude was calculated on the signal recorded by both EPDN and ECPN stations (Figure 3b), while the source location was obtained by means of a grid search method based on the joint computation of semblance function (which measures the similarity among signals recorded at different stations) and R^2 values (based on the calculation of the spatial distribution of seismic amplitudes) (Figure 5) [*Cannata et al*., 2013].

On the basis of both volcanic tremor and LP event features, we identified three periods of activity: (1) 1–20 August; (2) 21 August to 15 October; and (3) 16 October to 31 December. The first period was characterized by high amplitudes of both volcanic tremor and LP events related to the July–August eruptive fissure activity and to an explosive event at the NSEC. The volcanic tremor source centroid was located below the eastern flank of North-East Crater (NEC) up to 10 August when the eruptive fissure was active, and successively below NSEC, at very shallow depths (~2.5–3.0 km asl). The second period showed low amplitudes of both LP events and volcanic tremor, whose source centroids were located between NSEC and NEC at shallow depths of 2–3 km asl. Finally, during the third period we observed a gradual increase of the LP event amplitudes and a progressive migration of the tremor centroids toward the NEC at depths up to ~1 km asl. It is worth noting that it was not possible to verify prospective variations of the tremor source location during the 28 December lava fountain, because of the low number of properly working stations (Figure 4). Finally, during all the three periods, the sources of LP events were located below the summit craters at 2–3 km asl and did not show significant temporal changes (Figure 5).

3.1.2. Short-Term Analysis

A seismic short-term analysis was also carried out on data of 28 December 2014. The RMS time series of the vertical component of the EPDN station was calculated on nonoverlapping sliding 1 min long time windows (Figure 6a). The most obvious variation was a gradual increase of volcanic tremor amplitude at the same time as lava fountain activity started at ~14:00. At ~16:30 the increase in volcanic tremor amplitude became sharper, and the highest RMS values were reached between 17:20 and 18:20. During the following hours, volcanic tremor amplitude gradually decreased.

The number of seismic events during 28 December, within 10 min time windows, is reported in Figure 6b. A peculiar seismo-volcanic feature of this lava fountain was the increase in the rate of occurrence of seismic events during the initial phase (~16:00–17:00; see also Figure S1c) with the strongest event observed at 16:50. The lack of events after ~17:00–17:30 was partially due to the high amplitudes of volcanic tremor that prevented detecting possible small seismic events masked by the background noise.

With the exception of the 16:50 event, the detected transients were mainly characterized by emergent onsets, unclear *S* phases, and frequency content below 10 Hz (Figure S2). Such features suggested that these transients were LP events. On the other hand, the 16:50 event showed impulsive onsets and clear *S* phases (Figure S3). As for the spectral content, it was possible to observe a first part with higher frequency content than the coda (Figure S3). Since this characteristic was not observed at all the stations, it was not possible to clearly classify the 16:50 event. It was thus considered either a hybrid event or a shallow volcano tectonic earthquake (the so called VT-B) [*Wassermann*, 2012], with local magnitude of 3.0. However, in both cases (hybrid or VT-B event), a rock fracturing process is expected to have been involved.

The eight strongest seismic events taking place before the climax of the eruption (the 16:50 event and seven energetic LP events) were located using the HYPOELLIPSE software [*Lahr*, 1989]. Successively, such events were relocated using the tomoDDPS algorithm [*Zhang et al*., 2009] and the 3-D velocity model of *Alparone et al*. [2012]. Such method was used instead of the joint computation of semblance function and R^2, in order to obtain locations as precise as possible. Indeed, compared to other simpler algorithms, the tomoDDPS algorithm uses a combination of both absolute and differential arrival time readings between couple of events of an earthquake cluster. This essential feature allows considerably improving the relative locations. In fact, the use of the differential arrival times ensures that, for earthquake clusters with foci lying close to each other, the travel time errors due to incorrect velocity models in the volume outside the cluster will essentially be canceled out. The 3-D locations show that the weighted RMS residual decreases from 0.19 to 0.15 s, and the average location uncertainties (ERH and ERZ) are ~0.4 km. The results show that the considered seismic events tend to cluster in the depth range between 1.6 and 1.4 km asl, except for two ~800 m deeper events, one of which is that of 16:50 (Table 1).

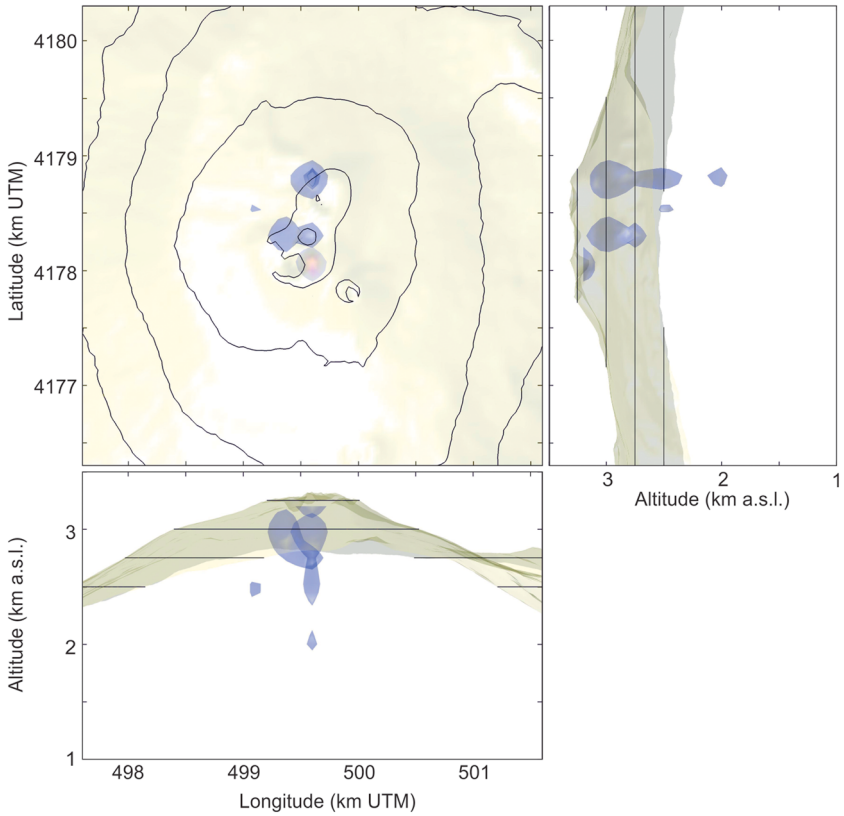

Figure 5. Map and sections of Etna with the source locations of LP events (blue surface) recorded during August–December 2014. The blue surface encloses all the grid nodes, used for the grid search location, with more than 500 LP event locations.

3.2. Geodetic Data

3.2.1. GPS Data

Daily raw observations collected from the permanent GPS network (Figure 1b) were analyzed using the GAMIT/GLOBK software [*Herring et al.*, 2010] and adopting the methodology described in the supporting information [*González and Palano*, 2014]. To detect signals related to the 28 December lava fountain, as well as during the months before the event, we analyzed the daily baseline changes between ECNE and EINT sites as they were quasi-continuously operating throughout the investigated period (Figure 3c). Since these stations are located northward (ECNE) and southward (EINT) of the summit crater area, their relative motion (e.g., baseline variation) over the time is sensitive to any deformation of the volcano summit. Visual inspection of the time series of the ECNE-EINT baseline length, spanning from 1 August to 31 December 2014, allowed detecting three different ground deformation stages (Figure 3c): (T1) from 1 to 21 August, the baseline shortened by ~0.7 cm, (T2) from 21 August up to 25 December, the baseline lengthened by ~1.5 cm, and apparently shortened by ~0.4 cm in the following 2 days (due to noisier acquisition at EINT), and (T3) from 27 to 29 December, the baseline lengthened by ~4.7 cm, well capturing the ground deformation field encompassing the 28 December lava fountain.

T1 reflects a depressurization of the plumbing system, as a consequence of the lava withdrawal related to the July–August 2014 eruptive fissure activity. In the following we focus on T2 and T3 by computing the 3-D deformation field of the GPS network. The 3-D deformation field related to T2 was computed in terms of geodetic velocities by combining the daily GAMIT solutions into a consistent set of station positions and velocities. To compute the amount of 3-D displacement during T3, we estimated the average site position in the 3 days preceding the event and in the 3 days following by applying minimal inner constraints (i.e., constraining translations, scale and rotations, to 0.1 mm). Estimated velocities/displacements for T2 and T3

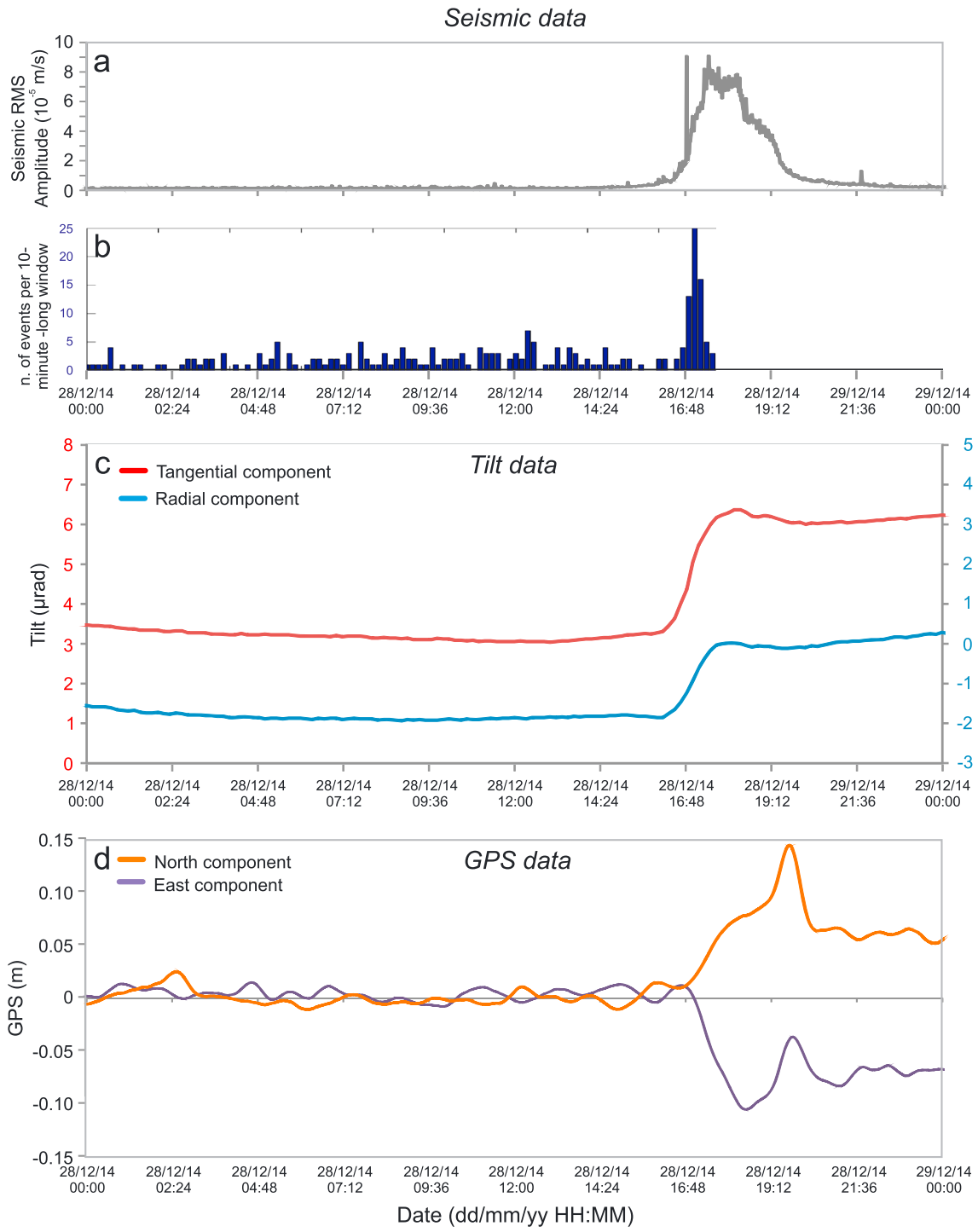

Figure 6. Variation in time of (a) seismic RMS at the vertical component of EPDN station, (b) of seismic events within 10 min long windows, (c) tangential and radial components of tilt at PDN long-base station, and (d) East and North component of EPDN GPS station during 28 December 2014.

were referred to a local reference frame (supporting information). The ground deformation field for T2 showed a general radial pattern of the computed surface velocities, clearly indicating pressurization of the volcano plumbing system (Figure 7). The deformation field occurring during T3 was captured by the stations closely located to the summit crater area, thus indicating a source that was confined at shallow depths (Figure 8).

Table 1. Progressive Number, Date, Origin Time, and Hypocentral Parameters of the Eight Seismic Events Relocated Using the tomoDDPS Algorithm and the 3-D Velocity Model [*Alparone et al.*, 2012][a]

No	Date[b]	Origin Time	Latitude (°N)	Longitude (°E)	Depth
1	2014/12/28	16:11:06.85	37.7481	15.0015	−1.56
2	2014/12/28	16:11:52.85	37.7497	15.0030	−1.56
3	2014/12/28	16:15:46.15	37.7493	14.9991	−0.51
4	2014/12/28	16:30:07.37	37.7503	14.9998	−1.42
5	2014/12/28	16:30:54.81	37.7543	15.0015	−1.44
6	2014/12/28	16:38:14.29	37.7519	15.0055	−1.61
7	2014/12/28	16:44:26.11	37.7481	15.0037	−1.57
8	2014/12/28	16:50:32.09	37.7454	15.0032	−0.68

[a]The main event at 16:50 has local magnitude $M_L = 3.0$.
[b]Dates are formatted as year/month/day.

3.2.2. Tilt Data

The permanent tilt network at Mount Etna comprises 13 instruments installed in shallow boreholes and one long-base instrument consisting of two orthogonal tubes filled with mercury positioned along two 80 m long tunnels at the Pizzi Deneri Observatory (PDN) (2850 m asl, Figure 1b) [*Ferro et al.*, 2011]. Tilt changes were systematically recorded during the tens of lava fountains occurring in the last decade [e.g., *Bonaccorso et al.*, 2011; *Patanè et al.*, 2013; *Gambino et al.*, 2014]. During the 2011–13 paroxysms, tilt variations generally ranged between 0.1 and 1.0 microradians [*Gambino et al.*, 2014]. The most obvious changes were visible on the radial components and showed deflation of the volcano edifice during the fountains [*Bonaccorso et al.*, 2011, 2013]. The 28 December 2014 episode differed from the others, because large variations (more than 3.0 microradians) were recorded at PDN station (Figure 6c), while the pattern of the other stations (Figure S4) showed a marked deflation tilt trend with respect to the 2011–2013 episodes. Starting from 14:00 slight changes were evident at CBD and CDV tilt stations, while all stations exhibited obvious changes of signals at ~16:00–16:20 (Figure S4). At PDN, the variation started at ~16:00, and showed the highest rate of deformation between 16:30 and 17:30, to return to normal values at ~19:00–19:30.

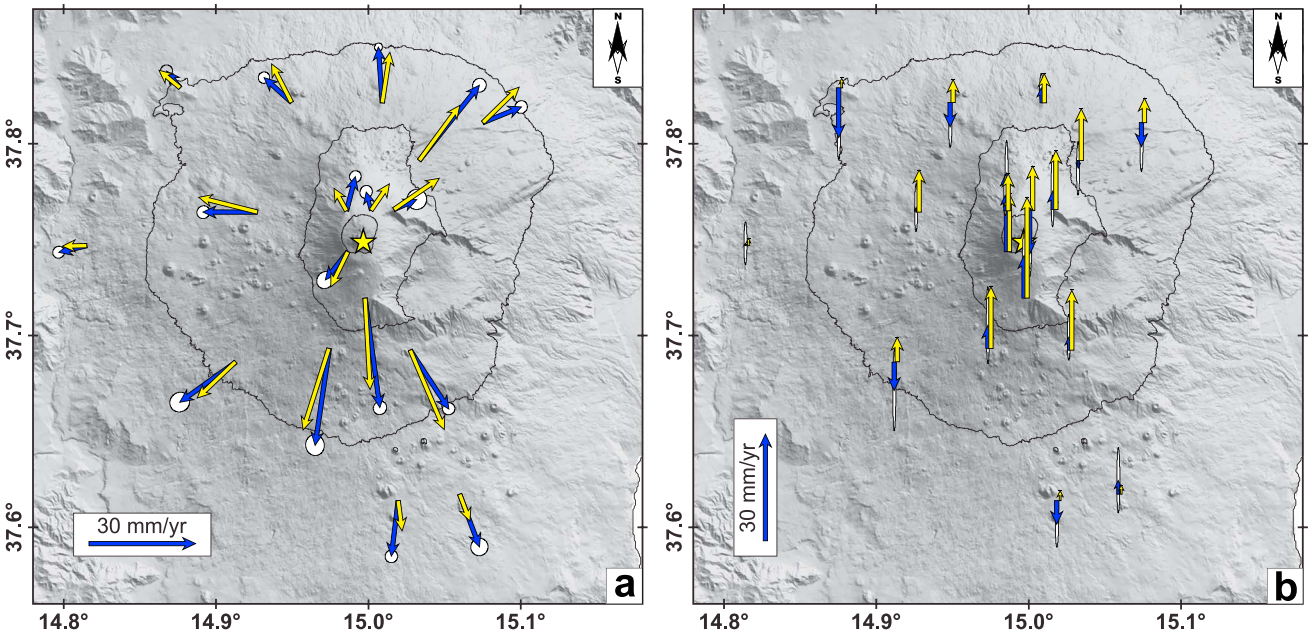

Figure 7. Comparison between the observed (blue arrows) and modeled (yellow arrows) (a) horizontal and (b) vertical geodetic velocities, relevant to T2 time interval (21 August to 25 December 2014). Uncertainties of the observed geodetic velocities are reported (with white ellipses) at the 95% level of confidences. The location of the modeled source is indicated with a yellow star. The parameters of this source are reported in Table 2.

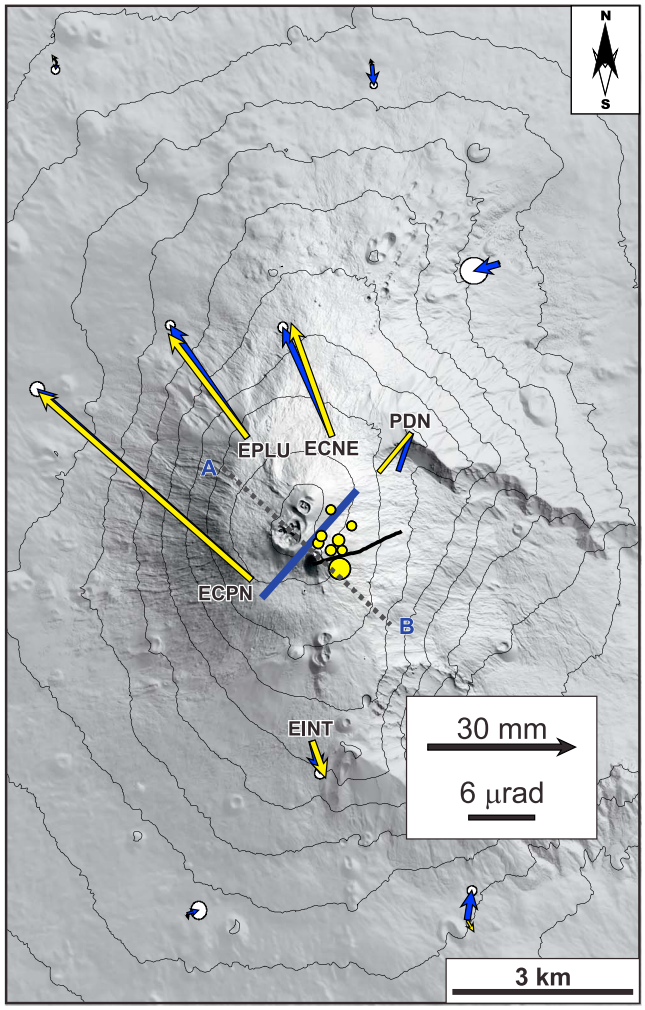

Figure 8. Comparison between the observed (blue arrows) and expected (yellow arrows) horizontal geodetic displacements, relevant to T3 time interval (27–29 December 2014). The amount of 3-D displacement during this time was estimated by averaging site position in the 3 days preceding the event and in the 3 days following it by applying minimal inner constraints. The modeled dike is traced with a dark blue line. The parameters of this source are reported in Table 2. Additionally, we indicate the eruptive fissure (black line). The yellow circles stand for seismic events locations (small circles: LP events taking place on 28 December at ~16:00–17:00; big circle: $M_L = 3$ event occurring on 28 December at 16:50) as described in section 3.1.2. The A–B dashed line indicates the section reported in Figure 10.

3.2.3. Geodetic Data Modeling

The surface ground deformation fields for T2 and T3 were inverted to constrain isotropic half-space elastic models. The inversions were performed using the genetic algorithm approach [*Tiampo et al.*, 2000] to minimize the misfit defined as the weighted root-mean-square error

$$\mathrm{WRMSE} = \sqrt{\sum_{i=1}^{n} \frac{(\hat{y}_i - y_i)^2}{n\sigma_i^2}} \quad (1)$$

where $\hat{y}_i$ is the predicted measures (either displacement or tilt components), y_i the observed ones, and σ_i^2 their associated errors.

Estimation of the uncertainties in best fitting parameters was performed by adopting a Jackknife sampling method [*Efron*, 1982] (Table 2). In the computation, both horizontal and vertical GPS components were inverted by taking into account the weights proportional to the associated errors.

Considering the radial pattern of the deformation field estimated for T2 and following the criterion described by *Cannavó* [2012], we selected the *Yang et al.* [1988] analytical pressure source to model it. In order to account for the effects of topography, we included into the computation the method of *Williams and Wadge* [2000]. We discarded all stations located on the middle to lower eastern flank of the volcano as affected by long-term seaward motion [e.g., *Palano et al.*, 2008]. The optimal model, which minimizes the weighted root-mean-square error (WRMSE) in (1), is given by a near vertical elongated ellipsoidal source centered beneath the summit craters at ~4.5 km below sea level (bsl) and with an estimated volume variation of $\sim 2.45 \times 10^6\ \mathrm{m}^3$ (Figure 7 and Table 2). The final result shows a reasonable fit (WRMSE = 22.8) between modeled and observed displacements (Figure 7). Locally, some mismatches in both 3-D direction and magnitude between the modeled and observed displacements can be seen. These are possibly linked to local effects, such as monument instability and/or motion along nearby active faults.

To model the deformation field estimated for T3, we selected the *Okada* [1985] analytical dislocation source as the model with the best fit to the data in terms of WRMSE. Due to the expected shallow depth of the modeled source, we did not take into account any topographic effect, as such effects cannot be properly resolved with the approximate solutions of *Williams and Wadge* [2000]. However, in our case the topography contribution can be considered negligible, as we used exclusively GPS stations close to summit crater area and with almost the same elevation for the inversion. In addition, we included in the inversion the tilt measurement at

Table 2. Parameters of the Modeled Sources Inferred for Time Intervals T2 and T3[a]

Parameters	T2	T3
Easting (m)	499710 ± 357	499774 ± 274
Northing (m)	4178005 ± 269	4178042 ± 518
Depth (m asl)	−4553 ± 683	2850 ± 209
a axis (m)	688 ± 136	
a/*b* ratio	0.210 ± 0.188	
Length (m)		2388 ± 286
Width (m)		832 ± 54
Azimuth (°)	28.7 ± 9.9	228 ± 2.8
Dip (°)	105 ± 3.0	89 ± 7.0
ΔV (Pa)	$1.63 \pm 0.3 \times 10^9$	
ΔV (10^6 m^3)	2.45	
Opening (m)		0.31 ± 0.13

[a] *a* and *b* are the lengths of the major and the minor axes of the spheroidal pressure source [*Yang et al*., 1988], respectively. ΔV is calculated as $\Delta V = \Delta P a b 2\pi/\mu$ according to *Tiampo et al*. [2000], where μ is the rigidity modulus of the elastic half-space. For each parameter, errors (at 95% of confidence) were estimated by adopting a Jackknife sampling method [*Efron*, 1982].

the PDN summit station (this was weighted as the GPS velocities). After some preliminary runs, we fixed the dip- and strike-slip components of the *Okada* [1985] dislocation source to zero because of their poor constraints. In this way, we also reduced the number of unknown parameters to be resolved by the inversion. The best model (WRMSE = 50.6) is given by a vertical 2.4 km long and 0.8 km wide dike located at a depth of ~2.85 km asl just beneath the NSEC-SEC area and characterized by an opening component of ~31 cm (Figure 8 and Table 2).

3.2.4. Time-Dependent Modeling

In order to analyze the volcano deformation during T3 at higher time resolution, we processed the GPS data in kinematic mode by using the TRACK software [*Herring et al*., 2010]. In the processing we chose station ENIC as reference (Figure 1b). The time series obtained after filtering with a 5 min sliding window was used to build a time-dependent model of the intruded dike. The previously modeled dike (Figure 8) was divided into a regular grid of patches. The analytical displacement due to each patch is linear in its opening component [*Okada*, 1985]; thus, following the superposition principle, we can write

$$du_i(p,t) = \sum_{s=1}^{Ns} \delta_{i^{(s)}}(p) \cdot \phi_s(t) \tag{2}$$

where $du_i(p,t)$ is the *i*th component of the vector displacement at the point *p* and the time *t*, *Ns* is the number of patches, $\delta_{i^{(s)}}(p)$ is the *i*th component of the vector displacement at the point *p* due to the unit opening of patch *s*, and $\phi_s(t)$ is the opening value of the patch *s* at the time *t*. We defined a time-space norm between two patches (s_1 and s_2) in two times (t_1 and t_2) as

$$\left\| s_1^{(t_1)}, s_2^{(t_2)} \right\| = \sqrt{\sum_i \left(\frac{s_{1i}^{(t_1)} - s_{2i}^{(t_2)}}{\sigma_a} \right)^2 + \left(\frac{t_1 - t_2}{\sigma_b} \right)^2} \tag{3}$$

where *i* is the *i*th component of the patch centroid and σ_a and σ_b are the two normalizing factors. As constraints, we considered for each patch a maximum allowable tensile value as the one found in the static model (i.e., $0 \le \phi_s(t) \le 0.3$). Moreover, we constrained the maximum variance between opening value of a patch *s* at time *t* and mean of time-space neighbor values

$$\left| \varphi_s(t) - \frac{1}{\left\| I_{(s,t)} \right\|} \sum (j,\tau) \in I_{(s,t)} \varphi_j(\tau) \right| < \phi_{\max} \tag{4}$$

where $I_{(s,t)}$ is the set of neighbor patches, $I_{(s,t)} = \left\{ (j,\tau) \neq (s,t) : \left\| s_{s^{(t)}}, s_{j^{(\tau)}} \right\| \le 1 \right\}$.

For our model we used the previously found dike, lengthened to avoid boundary effects and divided in a grid of 10×10 patches with σ_a as twice the diagonal length of a patch and σ_b as twice the minimum time step (15 min). We used the active-set algorithm [*Gill et al*., 1981] to solve the constrained linear least squares problem, obtaining the results shown in Figure 9 and in Movie S1 (supporting information). In particular, Figure 9 focuses on the time interval when the dike intruded (15:50–19:12) showing simultaneously (i) the opening distribution on the dike plane at five different times, (ii) the time series of measured and predicted displacement components recorded at the GPS stations, (iii) the RMS of the seismic signal recorded, and (iv) the occurrence of the main seismic events.

The time sequence shows a first intrusion in the eastern part of the SEC-NSEC fracture system (Figure 2) with a deep quasi-vertical feeding and deepening of the dike opening. This was followed at 17:30 by shallow migration of the intrusion toward the western portion of the fracture system, whose width did not exceed 400 m.

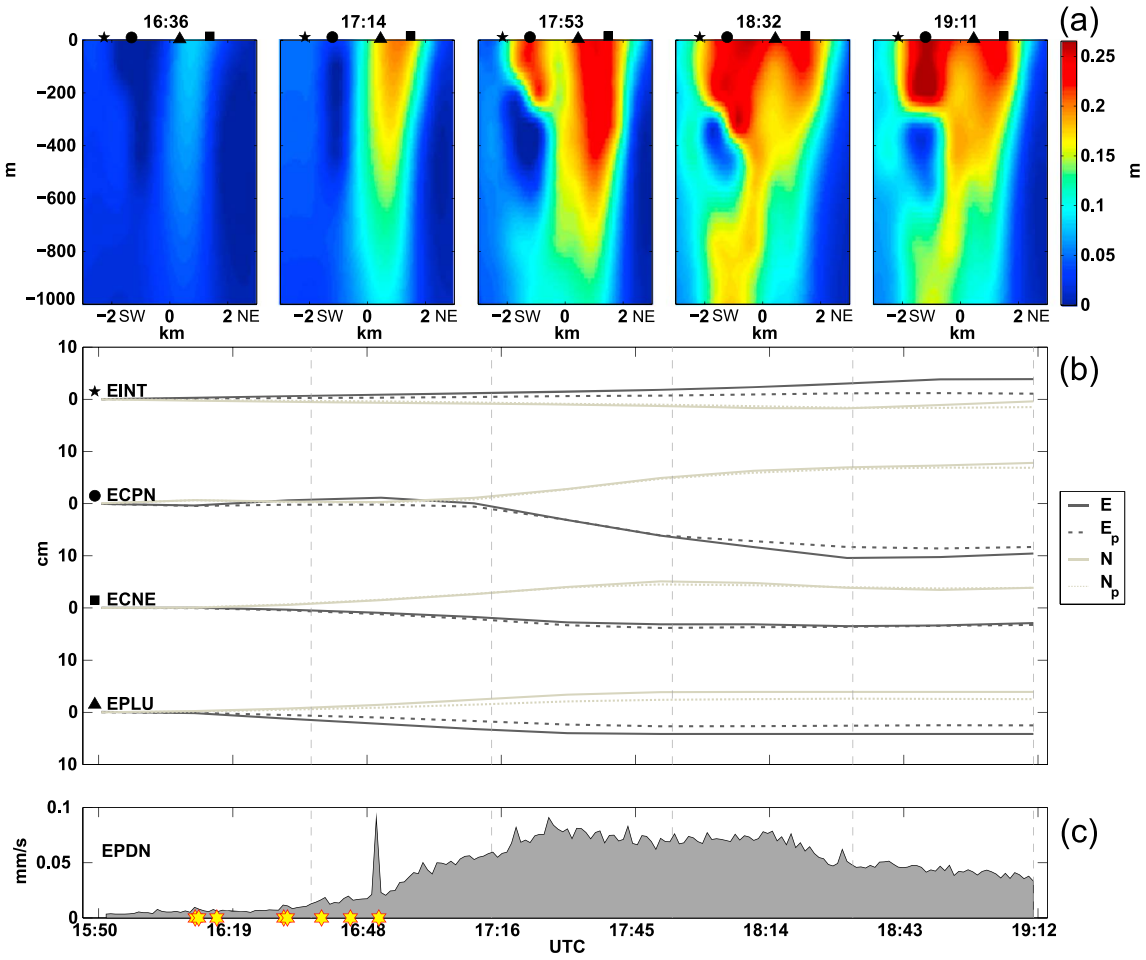

Figure 9. Results from the time-dependent modeling. (a) Opening distribution on the dike plane at five different times; black filled symbol refers to the four GPS stations, and their projection on the dike plane is shown. (b) Time series of the measured and predicted (dashed lines) displacement components recorded at the four GPS stations. (c) RMS of the seismic signal recorded at the vertical component of EPDN station; the yellow stars show the occurrences of the most powerful seismic events.

3.3. Geochemical Data

Assessment of the type and concentrations and fluxes of volcanic gases has provided significant insights into studying and modeling of magma ascent, transport, and degassing in volcanic plumbing systems [e.g., *Oppenheimer et al.*, 2003]. Volcanic gas emissions can provide insights into the degassing of ascending magma and its nature. For this reason, gas monitoring and study have proven to be critical for a better understanding of volcanic unrest phases [e.g., *Caltabiano et al.*, 2004] and for tracking the dynamics of volcanic activity [*Allard et al.*, 2005; *La Spina et al.*, 2015]. The dissolved volatiles exsolve from magma to form a separate gas phase (bubbles), in response to a pressure decrease during magma ascent and according to the characteristic saturation pressure of the single gas species; thus, every species will give an indication on the depth from which magma is degassing. In this paper, we consider the ratio between SO_2 and HCl that start to exsolve from parental magma at depths of <4 km and <2 km, respectively [*Spilliaert et al.*, 2006]. The SO_2/HCl molar ratio was determined using an open-path Fourier Transform Infrared spectrometer in solar occultation mode (supporting information).

From late September 2014, the SO_2/HCl ratio showed an increasing trend peaking with a value of 4 in the second half of November (Figure 3d). In December 2014, the ratio remained stable at high values (>3.5) to decrease in early January 2015 (Figure S5). At the end of January 2015, the ratio return to the values observed in September 2014. This trend marks the ascent and emplacement of undegassed magma in the shallower portion of the volcano. In particular, the period of increase of the ratio reflects progressive deficit in the

HCl degassing from the shallow magma system, connected to deeper derived gas bubbles, and less efficient convective motion of magma inside the upper conduit. On the contrary, in early January 2015, the decrease of the ratio and thus the predominance of HCl on SO_2 suggest efficient magma circulation at shallower conditions.

4. Results and Discussions

4.1. Timing and Mechanisms of the 28 December 2014 Lava Fountain

The paroxysmal event started abruptly in the afternoon of 28 December. However, the poor weather conditions prevented visual observation of the phenomenon, and the only evidences came from volcanic tremor and ash fallout and lava flows on the volcano flanks [*Bonforte and Guglielmino*, 2015]. Additional information was provided by the a posteriori processing of static and high-rate GPS and tilt data acquired by the summit stations. Volcanic tremor amplitude began to increase at ~14:00, and at 16:00–16:10 also the tilt and GPS signals showed clear changes indicating the onset of a dike intrusion (Figures 6c and 6d). Such a change in the ground deformation was accompanied by some strong LP events (Figure 6b). Starting from 16:30, the rate of deformation and the increase of the volcanic tremor amplitude intensified, and at 16:50 an $M_L = 3.0$ seismic event occurred. The event was probably due to the rock shear failure at depth in between 0 and 1 km asl, caused by the changes in local stress field generated by the dike intrusion, as previously observed at Mount Etna [e.g., *Gambino*, 2004; *Bonanno et al*., 2011]. From 18:20, both volcanic tremor amplitude and ground deformation gradually decreased until 19:00–19:30, when the lava fountain eventually ended. During the fountain, two distinct lava flow fields developed from the opposite tips of the NE-SW trending eruptive fissure that opened in the fractured area between SEC and NSEC as the shallow response to the dike intrusion [*Bonforte and Guglielmino*, 2015] (inset in Figure 1a).

The occurrence of considerable horizontal displacements at stations close to the summit area (up to 10 cm at ECPN station; Figure 8) allowed us to develop isotropic elastic models to infer the geometry and position of the dike feeding the lava fountain, as well as the temporal and spatial variation of its opening component. Modeling of the GPS data inferred a shallow dike crossing the SEC-NSEC saddle (Figure 8), with similar depth and azimuth to the one proposed by *Bonforte and Guglielmino* [2015], although different in the size (~0.5 km wider in plunge direction and ~1.6 km longer in strike direction) and kinematics. Regarding this last feature, our best model is characterized by a tensile component of ~0.31 m, while the one proposed by *Bonforte and Guglielmino* [2015] shows a left-lateral reverse fault kinematics, with a slip of 2.3 m and a tensile component of 5.6 m.

Our best model results in a WRMSE of 50.6, which is a much lower value when compared with the one obtained using the model parameters inferred by *Bonforte and Guglielmino* [2015] (i.e., 327.1). Such a difference might be due to the partially different set of GPS data used as input for constraining the models (i.e., *Bonforte and Guglielmino* included also measurements from GPS campaigns, while we included instead continuous tilt data) and to the different time intervals covered by the modeled deformation pattern. Regarding the time interval, it must be noted that our data set covers the 27–29 December 2014 period, while *Bonforte and Guglielmino* [2015] cover the time window between July 2014 and January 2015. Such a longer time interval includes the cumulative effects of different sources—i.e., a deflating source active from 1 August to 21 August 2014 (Figure 2), an inflating source from 21 August to 27 December 2014 (Figures 2 and 7), and the dike intrusion of 28 December 2014 (Figures 2 and 8). The use of tilt data allowed us to better constrain the position of the modeled dike. In this way, different from *Bonforte and Guglielmino* [2015], our modeled dike is located just beneath the fracture field between SEC-NSEC. Moreover, considering the fracture field extension and seismic event location, our wider and longer dike seems more reasonable (Figures 8 and 9).

As far as the temporal and spatial variation is concerned, the time-dependent modeling allowed us to inferring the opening component of the intruding dike (Figure 9). The vertical upraise of the dike started around 16:30 and was accompanied by the increase of volcanic tremor amplitude and of the occurrence of the seismic events. The time-dependent modeling evidenced that the northern sector of the dike opened initially and for its entire width, and after 17:15 the upper portion of its southern sector started to open too. After 17:45, the ECNE and EPLU stations located northward to the fracture field showed no significant deformation, while the ECPN station sited westward to the fracture field significantly deformed until ~18:30. The behavior of these stations, coupled with the other independent observations previously reported, suggests that

1. the onset of the dike intrusion was accompanied by amplitude increase of the volcanic tremor and the occurrence of LP events (Figures 6a and 6b). Although the increase of the volcanic tremor amplitude is a common feature to all Mount Etna's lava fountains [e.g., *Viccaro et al*., 2014; *La Spina et al*., 2015], the LP activity intensification is unusual. These LP events, located just below the base of the intrusion, can here be attributed to geometrical discontinuities (such as changes in conduit diameter, pipe elbow, interlocking cracks, and so on) [e.g., *James et al*., 2006; *Chouet et al*., 2010] of the SEC-NSEC shallow feeding system likely "modified" by the dike intrusion. The lack of LP activity increase during the previous lava fountains was probably due to the ascent of gas-rich magma that took place through the well-established plumbing system of NSEC and not to dike intrusion;
2. while approaching the surface, magma first migrated laterally toward SW and fed the western lava flow, and then it fed lava fountaining and the eastern lava flow;
3. the time interval, when the eruptive fissure propagated southwestward, coincided with the period of maximum amplitude of volcanic tremor at 17:30 (Figure 9 and Movie S1 in the supporting information). Given that during explosive activity volcanic tremor amplitude positively correlates to the intensity of the eruptive phenomena [e.g., *Alparone et al*., 2003], we may deduce that the fissure propagation took place at the same time as the lava fountain episode climaxed.

4.2. What Made the 28 December 2014 Lava Fountain Different From the Previous Episodes?

While analyzing the mechanisms of the 28 December 2014 feeding dike intrusion, a key question arose: why a dike intrusion? All the 2011–2013 NSEC lava fountains were, in fact, interpreted as resulting from the well-known foam collapse model [e.g., *Calvari et al*., 2011], frequently used to explain lava fountains at Mount Etna, and thus were not associated with dike intrusions [e.g., *Parfitt*, 2004; *Allard et al*., 2005; *Vergniolle and Ripepe*, 2008; *Calvari et al*., 2011; *La Spina et al*., 2015]. In this frame, we attempted to find the mechanism that triggered the difference between this lava fountain and the previous NSEC-fed events. Indeed, after 43 lava fountains, we expected the NSEC shallow feeding system to be well structured and stabilized, so what was the reason for its likely structural modification? To answer this question, we tried to set the 28 December event within the framework of all the NSEC eruptive activity. Indeed, the 28 December lava fountain occurred after a year, during which the NSEC modified its eruptive style, shifting from sequences of intense lava fountaining in 2011–2013 to Strombolian activity accompanied by lava output that never climaxed in lava fountaining [e.g., *De Beni et al*., 2015]. In July–August 2014 the discontinuous eruptive activity of NSEC was supplanted by the opening of an eruptive fissure eastward from NEC that fed Strombolian explosions and lava flows [*De Beni et al*., 2015]. The activity at the fissure was not triggered by dike intrusion but was likely correlated to the NSEC system. The connection between the two systems was evident while considering that the crater summit activity stopped as soon as the fissure established and renewed almost when the fissure sealed (Figure 3a). Our hypothesis was confirmed by *De Beni et al*. [2015], who assessed the connection between NSEC and the eruptive fissure by observing the fracture system that developed in that area. As a result, we can infer that after the high intensity of the last 2013 lava fountains [e.g., *Spampinato et al*., 2015], a volatile depletion of the magma batch supplying the NSEC shallow plumbing system occurred. This likely promoted sporadic Strombolian activity centered at NSEC and drainage of the volatile depleted magma from a lower zone, which was already affected by the eruptive fissure opening in 2008–2009 [e.g., *Aloisi et al*., 2011]. Petrological analysis evidenced that the composition of the products erupted by NSEC between January and August 2014 was homogeneous and comparable to those erupted starting from 2011 (Corsaro and Miraglia, unpublished data). On the other hand, the composition of the products of the eruptive fissure was more evolved with respect to the NSEC ones, thus suggesting that the shift of the eruptive activity from NSEC to the fissure was not associated with the arrival of more primitive batches of magma in the volcano shallow feeding system (Corsaro and Miraglia, unpublished data).

Magma drainage from the eruptive fissure likely caused destabilization of the NSEC summit system due to conduit emptying that was observable at the surface by the further development of the fracture system that had previously formed between the NSEC and SEC summits (Figure 2), and by subsidence of the NSEC inner summit (Figure 2b). The progressive effusion through the fissure then promoted the rise of another volatile-rich batch magma. This was at first detected by the GPS observations that, starting from August 2014, recorded the pressurization of a deep portion of the Mount Etna plumbing system (Figure 3d). Modeling of these data, over the August–December 2014 interval, infers a pressurizing magma source with a vertically

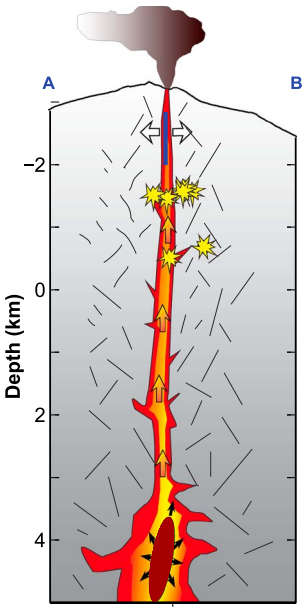

Figure 10. The schematic NW-SE section (A–B dashed line in Figure 8) crosses the summit area of Mount Etna and shows the modeled sources and located seismicity. The red ellipse shows the vertical elongated ellipsoidal pressure source modeled with the deformation data recorded during 21–25 December 2014 (phase T2). The yellow stars indicate the hypocenters of the seismic events that occurred on 28 December 2014 at ~16:00–17:00. The blue vertical line shows the dike modeled by using the GPS and tilt data during the phase T3.

elongated ellipsoidal shape located at a depth of ~4.5 km bsl beneath the summit craters (Figure 10), matching well the location of the 2008–2009 eruption magma sources [e.g., *Aloisi et al.*, 2011; *Patanè et al.*, 2013]. From the end of September, the pressurization became evident in the geochemical data as suggested by the increase of the SO_2/HCl ratio indicating deeper magma degassing and shallow accumulation of magma, potentially refilling the NSEC system (Figure 3e). From mid-October, pressurization was also observable from the progressive increase of the LP event amplitudes (Figure 3c) and as a gradual migration of the tremor centroids toward NEC and at deeper depth (1–2 km asl; Figure 4). Indeed, the increase in LP amplitudes has been interpreted as caused by pressurization of the volcano plumbing system that sometimes preceded eruptions [*Moran et al.*, 2008; *Bonaccorso et al.*, 2011; *Cannata et al.*, 2015], while the volcanic tremor source volume below NEC at 1–2 km asl was considered representative of the shallower magma storage zone, feeding the 2011 episodic fountaining activity [*Patanè et al.*, 2013]. The ascent of magma at shallow depths further destabilized the NSEC shallow plumbing system, thus promoting the emplacement of a dike-like structure. Hence, magma reached shallower depths by avoiding the pathways previously used to feed the 2011–2013 fountains. Dike emplacement was accompanied by low seismicity, and the volcanic tremor source variations suggested that the shallower pressurization involved the same magma storage zone that fed the previous lava fountain episodes [*Patanè et al.*, 2013]. Based on these observations, we can infer that dike emplacement cannot be attributed to a proper "intrusion" from depth as it was for instance in 2001, 2002, or 2008 [*Acocella and Neri*, 2003; *Andronico et al.*, 2005; *Aloisi et al.*, 2011]. In our case, the dike formed mainly due to shallow external effects that were not related to deep supply mechanisms but likely to morphological/structural modifications of the NSEC shallow feeding system. At the surface, the dike induced the development of an eruptive fissure in the fractured zone previously observed between SEC and NSEC. The azimuth difference between the modeled dike (N48°E) and the eruptive fracture field (N75°E) suggests that the preexisting fractures were shallow and were involved by the intrusive process only in the final stage.

5. Concluding Remarks

The combination between geophysical and geochemical data and their comparison and integration with previous observations of Mount Etna's eruptive activity allowed us to characterize and model the 28 December 2014 lava fountain episode, as well as constrain the likely mechanisms on the basis of its onset. Our main findings can be summarized as follows.

1. According to the geodetic data, the 28 December lava fountain was preceded by the pressurization of both deep and shallow portions of Mount Etna's plumbing system. In particular, modeling of the GPS data inferred a pressure source that was active from late August, which was located beneath the volcano summit area at depths of ~4.5 km bsl and that induced an estimated volume variation of ~2.45×10^6 m^3.
2. From September to October, such a variation was observed by seismic and geochemical data that highlighted pressurization of the shallower portion of the plumbing system;

3. the 28 December eruptive event was characterized by the emplacement of a shallow dike, which fed lava fountaining and lava output from an ENE-WSW trending eruptive fissure; this fissure opened between the SEC and NSEC summits and partially retraced the fracture system observable at the surface at least from early January 2014.
4. The time-dependent model of the tensile component of the dike provided evidence of a vertical ascent of magma (from 16:30 to 17:15) followed by a southwestward migration (after 17:15), when it interacted with the preexisting ENE-WSW fracture field. Such an interpretation explains well the occurrence of two distinct lava flows spreading in different directions.
5. Moreover, except for the seismic event recorded just before the start of the lava fountain, no significant seismic activity that might have suggested a deep intrusion process was recorded. Therefore, we believe that the 28 December 2014 dike emplacement resulted from a modification of the preexisting NSEC shallow pluming system (~1 km depth below the summit area), mainly due to its relative emptying for magma drainage through the July–August 2014 eruptive fissure activity. Such a structural modification might have created the conditions for which the rising magma emplaced as a dike-like structure. This evidence accords well with the geochemical data, which suggest that the lava fountain resulted from the accumulation and collapse of a foam layer within the NSEC shallow feeding system.

Acknowledgments
We thank the Editor, André Revil, and two anonymous reviewers for their insightful comments and suggestions, which helped improve the manuscript. We are indebted to the technicians of the INGV-Osservatorio Etneo for enabling the acquisition of seismic, tilt, and GPS data. We are grateful to E.P. Pratticò for the stimulating discussion which greatly improved this study. We also thank S. Conway for correcting and improving the English language of this manuscript. The data for this paper are available by contacting the corresponding author (salvatore.gambino@ingv.it).

References

Acocella, V., and M. Neri (2003), What makes flank eruptions? The 2001 Etna eruption and its possible triggering mechanisms, *Bull. Volcanol.*, *65*, 517–529.

Allard, P., M. Burton, and F. Murè (2005), Spectroscopic evidence for a lava fountain driven by previously accumulated magmatic gases, *Nature*, *433*, 407–410.

Aloisi, M., A. Bonaccorso, F. Cannavò, S. Gambino, M. Mattia, G. Puglisi, and E. Boschi (2009), A new dike intrusion style for the Mount Etna May 2008 eruption modelled through continuous tilt and GPS data, *Terra Nova*, *21*, 316–321, doi:10.1111/j.1365-3121.2009.00889.x.

Aloisi, M., M. Mattia, C. Ferlito, M. Palano, V. Bruno, and F. Cannavò (2011), Imaging the multi-level magma reservoir at Mt. Etna volcano (Italy), *Geophys. Res. Lett.*, *38*, L16306, doi:10.1029/2011GL048488.

Alparone, S., D. Andronico, L. Lodato, and T. Sgroi (2003), Relationship between tremor and volcanic activity during the Southeast Crater eruption on Mount Etna in early 2000, *J. Geophys. Res.*, *108*(B5), 2241, doi:10.1029/2002JB001866.

Alparone, S., G. Barberi, O. Cocina, E. Giampiccolo, C. Musumeci, and D. Patanè (2012), Intrusive mechanism of the 2008-2009 Mt. Etna eruption: Constraints by tomographic images and stress tensor analysis, *J. Volcanol. Geotherm. Res.*, *229–230*, 50–63.

Andronico, D., and R. A. Corsaro (2011), Lava fountains during the episodic eruption of South-East Crater Mt. Etna, 2000: Insights into magma-gas dynamics within the shallow volcano plumbing system, *Bull. Volcanol.*, *73*(9), 1165–1178, doi:10.1007/s00445-011-0467-y.

Andronico, D., and L. Lodato (2005), Effusive activity at Mount Etna volcano (Italy) during the 20th century: A contribution to volcanic hazard assessment, *Nat. Hazards*, *36*, 407–443, doi:10.1007/s11069-005-1938-2.

Andronico, D., et al. (2005), A multi-disciplinary study of the 2002-03 Etna eruption: Insights into a complex plumbing system, *Bull. Volcanol.*, *67*, 314–330.

Andronico, D., A. Cristaldi, and S. Scollo (2008), The 4-5 September 2007 lava fountain at South-East Crater of Mt Etna, Italy, *J. Volcanol. Geotherm. Res.*, *173*, 325–328.

Andronico, D., S. Scollo, A. Cristaldi, and F. Ferrari (2009), Monitoring ash emission episodes at Mt. Etna: The 16 November 2006 case study, *J. Volcanol. Geotherm. Res.*, *180*, 123–134.

Behncke, B., S. Branca, R. A. Corsaro, E. De Beni, L. Miraglia, and C. Proietti (2014), The 2011–2012 summit activity of Mount Etna: Birth, growth and products of the new SE crater, *J. Volcanol. Geotherm. Res.*, *270*, 10–21.

Bonaccorso, A., and S. Calvari (2013), Major effusive eruptions and recent lava fountains: Balance between expected and erupted magma volumes at Etna volcano, *Geophys. Res. Lett.*, *40*, 6069–6073, doi:10.1002/2013GL058291.

Bonaccorso, A., et al. (2011), Dynamics of a lava fountain revealed by geophysical, geochemical and thermal satellite measurements: The case of the 10 April 2011 Mt Etna eruption, *Geophys. Res. Lett. 38*, L24307, doi:10.1029/2011GL049637.

Bonaccorso, A., S. Calvari, G. Currenti, C. Del Negro, G. Ganci, A. Linde, R. Napoli, R. Sacks, and A. Sicali (2013), From source to surface: Dynamics of Etna's lava fountains investigated by continuous strain, magnetic, ground and satellite thermal data, *Bull. Volcanol.*, *75*, 690, doi:10.1007/s00445-013-0690-9.

Bonanno, A., M. Palano, E. Privitera, S. Gresta, and G. Puglisi (2011), Magma intrusion mechanisms and redistribution of seismogenic stress at Mt. Etna volcano (1997–1998), *Terra Nova*, *23*, 339–348, doi:10.1111/j.1365-3121.2011.01019.x.

Bonforte, A., and F. Guglielmino (2015), Very shallow dike intrusion and potential slope failure imaged by ground deformation: The 28 December 2014 eruption on Mount Etna, *Geophys. Res. Lett.*, *42*, 2727–2733, doi:10.1002/2015GL063462.

Branca, S., and P. Del Carlo (2005), Types of eruptions of Etna volcano AD 1670-2003: Implications for short-term eruptive behaviour, *Bull. Volcanol.*, *67*, 732–742, doi:10.1007/s00445-005-0412-z.

Burton, M. R., et al. (2005), Etna 2004-2005: An archetype for geodynamically-controlled effusive eruptions, *Geophys. Res. Lett.*, *32*, L09303, doi:10.1029/2005GL022527.

Caltabiano, T., M. Burton, S. Giammanco, P. Allard, N. Bruno, F. Murè, and R. Romano (2004), Volcanic gas emissions from the summit craters and flanks of Mt. Etna, 1987–2000, in *Mt. Etna: Volcano Laboratory*, *AGU Geophys. Monogr. Ser. 01/2003; Mt. Etna: Volcano Laboratory*, vol. 143, edited by A. Bonaccorso, pp. 111–128, AGU, Washington, D. C.

Calvari, S., G. G. Salerno, L. Spampinato, M. Gouhier, A. La Spina, E. Pecora, A. J. L. Harris, P. Labazuy, E. Biale, and E. Boschi (2011), An unloading foam model to constrain Etna's 11–13 January 2011 lava fountaining episode, *J. Geophys. Res.*, *116*, B11207, doi:10.1029/2011JB008407.

Cannata, A., M. Hellweg, G. Di Grazia, S. Ford, S. Alparone, S. Gresta, P. Montalto, and D. Patanè (2009), Long period and very long period events at Mt. Etna volcano: Characteristics, variability and causality, and implications for their sources, *J. Volcanol. Geotherm. Res.*, *187*(3), 227–249.

Cannata, A., G. Di Grazia, M. Aliotta, C. Cassisi, P. Montalto, and D. Patanè (2013), Monitoring seismo-volcanic and infrasonic signals at volcanoes: Mt. Etna case study, *Pure Appl. Geophys.*, *170*(11), 1751–1771, doi:10.1007/s00024-012-0634-x.

Cannata, A., G. Spedalieri, B. Behncke, F. Cannavò, G. Di Grazia, S. Gambino, S. Gresta, S. Gurrieri, M. Liuzzo, and M. Palano (2015), Pressurization and depressurization phases inside the plumbing system of Mount Etna volcano: Evidence from a multiparametric approach, *J. Geophys. Res. Solid Earth*, *120*, 5965–5982, doi:10.1002/2015JB012227.

Cannavó, F. (2012), Sensitivity analysis for volcanic source modeling quality assessment and model selection, *Comput. Geosci.*, *44*, 52–59, doi:10.1016/j.cageo.2012.03.008.

Chouet, B. A., P. B. Dawson, M. R. James, and S. J. Lane (2010), Seismic source mechanism of degassing bursts at Kilauea Volcano, Hawaii: Results from waveform inversion in the 10–50 s band, *J. Geophys. Res.*, *115*, B09311, doi:10.1029/2009JB006661.

De Beni, E., B. Behncke, S. Branca, I. Nicolosi, R. Carluccio, F. D'Ajello Caracciolo, and M. Chiappini (2015), The continuing story of Etna's New Southeast Crater (2012-2014): Evolution and volume calculations based on field surveys and aerophotogrammetry, *J. Volcanol. Geotherm. Res.*, *303*, 175–186.

Efron, B. (1982), *The Jackknife, Bootstrap and Other Resampling Plans*, Soc. of Ind. and Appl. Math., Philadelphia, Pa.

Ferro, A., S. Gambino, S. Panepinto, G. Falzone, G. Laudani, and B. Ducarme (2011), High precision tilt observation at Mt. Etna Volcano, Italy, *Acta Geophys.*, *59*(3), 618–632.

Gambino, S. (2004), Continuous dynamic response along a pre-existing structural discontinuity induced by the 2001 eruption at Mt Etna, *Earth Planets Space*, *56*, 447–456.

Gambino, S., G. Falzone, A. Ferro, and G. Laudani (2014), Volcanic processes detected by tiltmeters: A review of experience on Sicilian volcanoes, *J. Volcanol. Geotherm. Res.*, *271*, 43–54.

Gill, P. E., W. Murray, and M. H. Wright (1981), *Practical Optimization*, Academic Press, London, U. K.

González, P. J., and M. Palano (2014), Mt. Etna 2001 eruption: New insights into the magmatic feeding system and the mechanical response of the western flank from a detailed geodetic dataset, *J. Volcanol. Geotherm. Res.*, *274*, 108–121, doi:10.1016/j.jvolgeores.2014.02.001.

Gouhier, M., A. J. L. Harris, S. Calvari, P. Labazuy, Y. Guéhenneux, F. Donnadieu, and S. Valade (2012), Lava discharge during Etna's January 2011 fire fountain tracked using MSG-SEVIRI, *Bull. Volcanol.*, *74*, 787–793, doi:10.1007/s00445-011-0572-y.

Herring, T. A., R. W. King, and S. C. McClusky (2010), *Introduction to GAMIT/GLOBK, Release 10.4*, pp. 1–48, Mass. Inst. of Technol., Cambridge, Mass.

James, M. R., S. J. Lane, and B. A. Chouet (2006), Gas slug ascent through changes in conduit diameter: Laboratory insights into a volcano-seismic source process in low-viscosity magmas, *J. Geophys. Res.*, *111*, B05201, doi:10.1029/2005JB003718.

La Spina, A., M. Burton, P. Allard, S. Alparone, and F. Murè (2015), Open-path FTIR spectroscopy of magma degassing processes during eight lava fountains on Mount Etna, *Earth Planet. Sci. Lett.*, *413*, 123–134, doi:10.1016/j.epsl.2014.12.038.

Lahr, J. C. (1989), HYPOELLIPSE/VERSION 2.0: A computer program for determining local earthquake hypocentral parameters, magnitude and first motion pattern, *U.S. Geol. Surv. Open File Rep.*, *89*(116), 1-81.

Moran, S. C., S. D. Malone, A. I. Qamar, W. A. Thelen, A. K. Wright, and J. Caplan-Auerbach (2008), Seismicity associated with the renewed dome-building eruption of Mount St. Helens 2004–2005, in *A Volcano Rekindled: The Renewed Eruption of Mount St. Helens, 2004–2006*, *U.S. Geol. Surv. Prof. Pap.*, vol. 1750, edited by D. R. Sherrod, W. E. Scott, and P. H. Stauffer, pp. 27–54, Reston, Va.

Okada, Y. (1985), Surface deformation due to shear and tensile fault in half-space, *Bull. Seismol. Soc. Am.*, *75*, 1135–1154.

Oppenheimer, C., D. M. Pyle, and J. Barclay (2003), Volcanic degassing, *Geol. Soc. Spec. Publ.*, *213*, 1–3.

Palano, M., G. Puglisi, and S. Gresta (2008), Ground deformation patterns at Mt. Etna from 1993 to 2000 from joint use of InSAR and GPS techniques, *J. Volcanol. Geotherm. Res.*, *169*(3–4), 99–120, doi:10.1016/j.jvolgeores.2007.08.014.

Parfitt, E. A. (2004), A discussion of the mechanisms of explosive basaltic eruptions, *J. Volcanol. Geotherm. Res.*, *134*, 77–107.

Patanè, D., et al. (2013), Insights into magma and fluid transfer at Mount Etna by a multiparametric approach: A model of the events leading to the 2011 eruptive cycle, *J. Geophys. Res. Solid Earth*, *118*, 3519–3539, doi:10.1002/jgrb.50248.

Spampinato, L., S. Calvari, C. Oppenheimer, and L. Lodato (2008), Shallow magma transport for the 2002-3 Mt. Etna eruption inferred from thermal infrared surveys, *J. Volcanol. Geotherm. Res.*, *177*, 301–312.

Spampinato, L., M. Sciotto, A. Cannata, F. Cannavò, A. La Spina, M. Palano, G. G. Salerno, E. Privitera, and T. Caltabiano (2015), Multi-parametric study of the February-April 2013 paroxysmal phase of Mt. Etna New South-East crater, *Geochem. Geophys. Geosyst.*, *16*, 1932–1949, doi:10.1002/2015GC005795.

Spilliaert, N., N. Métrich, and P. Allard (2006), S-Cl-F degassing pattern of water rich alkali basalt: Modelling and relationship with eruption styles of Mount Etna volcano, *Earth Planet. Sci. Lett.*, *248*, 772–786.

Tiampo, K. F., J. B. Rundle, J. Fernandez, and J. O. Langbein (2000), Spherical and ellipsoidal volcanic sources at Long Valley Caldera, California, using a genetic algorithm inversion technique, *J. Volcanol. Geotherm. Res.*, *102*, 189–206, doi:10.1016/S0377-0273(00)00185-2.

Vergniolle, S., and M. Ripepe (2008), From Strombolian explosions to fire fountains at Etna volcano (Italy): What do we learn from acoustic measurements?, *Geol. Soc. London Spec. Publ.*, *307*, 103–124.

Viccaro, M., I. Garozzo, A. Cannata, G. Di Grazia, and S. Gresta (2014), Gas burst vs. gas-rich magma recharge: A multidisciplinary study to reveal factors controlling duration of the recent paroxysmal eruptions at Mt. Etna, *J. Volcanol. Geotherm. Res.*, *278–279*, 1–13.

Wassermann, J. (2012), *Volcano Seismology, IASPEI New Manual of Seismological Observatory Practice 2 (NMSOP-2)*, 2nd ed., edited by P. Bormann, 1–77, Deutsches GeoForschungsZentrum GFZ, Potsdam, Potsdam, doi:10.2312/GFZ.NMSOP-2_ch13.

Williams, C. A., and G. Wadge (2000), An accurate and efficient method for including the effects of topography in three-dimensional elastic models of ground deformation with applications to radar interferometry, *J. Geophys. Res.*, *105*(B4), 8103–8120, doi:10.1029/1999JB900307.

Yang, X.-M., P. M. Davis, and J. H. Dieterich (1988), Deformation from inflation of a dipping finite prolate spheroid in an elastic half-space as a model for volcanic stressing, *J. Geophys. Res.*, *93*, 4249–4257, doi:10.1029/JB093iB05p04249.

Zhang, H., C. Thurber, and P. Bedrosian (2009), Joint inversion for Vp, Vs, and Vp/Vs at SAFOD, Parkfield, California, *Geochem. Geophys., Geosyst.*, *10*, Q110032, doi:10.1029/2009GC002709.